

Supplemental Information

Amphiphilic Engineering of MoS₂-g-C₃N₄ Nanocomposites into a Mangrove-Inspired Cascade System for Sustainable Drinking Water Production

Sichen Liu^{a,#}, Haotian Wang^{a,#}, Yumeng Xiao^a, David G. Calatayud^b, Boyang Mao^c, Gaoqi Zhang^d, Chenhui Yang^d, Lidong Wang^a, Meng Li^{a,*}

^a Hebei Key Lab of Power Plant Flue Gas Multi-Pollutants Control, Department of Environmental Science and Engineering, North China Electric Power University, Baoding, 071003, P. R. China

^b Department of Electroceramics, Instituto de Ceramica y Vidrio CSIC, Kelsen 5, Campus de Cantoblanco, Madrid, 28049, Spain

^c Department of Engineering, University of Cambridge, Cambridge, CB3 0FA, U. K.

^d Key Laboratory of Bio-based Material Science and Technology of Ministry of Education, Material Science and Engineering College, Northeast Forestry University, Hexing Road 26, Harbin, 150040, P. R. China

indicates the co-first author.

*Corresponding authors. E-mail: mlincepu@hotmail.com

1. Experimental Section

1.1 Materials characterizations

SEM images were acquired using an S-4800 field-emission scanning electron microscope (Hitachi, Japan) at magnifications ranging from 2500 to 100,000. The morphology and structure of the specimen were examined using a JEM-2100 transmission electron microscope (TEM) operating at an acceleration voltage of 200 kV. Analysis of surface elements and functional groups on the adsorbent was conducted using X-ray photoelectron spectroscopy (XPS, ESCALAB 250Xi) with resolutions of 0.48 eV (Ag 3d5/2) and 0.68 eV (C 1s), respectively. UV-visible absorption spectra were recorded using the Beijing Puxi T6 New Century UV-visible spectrophotometer. AFS-933 atomic fluorescence photometer and ICP-OES were used to measure the Hg^{2+} , Cu^{2+} , Pb^{2+} , Cd^{2+} concentration in the solution.

1.2 Adsorption experiments

The static adsorption capacity of MoG composite was evaluated by analyzing the reduction of cationic dye Rhodamine B, anionic dye Congo Red and Hg^{2+} in aqueous solution. In the context of static adsorption investigations, a quantity of 10 mg of the adsorbent was introduced into 10 mL of distinct contaminant solutions characterized by initial concentrations ranging from 10 to 500 mg L^{-1} , and the system was allowed to equilibrate for a duration of 2 hours. Subsequently, the remaining dye content within the solution was quantified using ultraviolet spectroscopy, while the concentration of Hg^{2+} was ascertained through atomic fluorescence spectroscopy. Furthermore, the impact of varying contact durations (0-120 min) as well as temperatures (25-65 °C)

were methodically explored, while maintaining a constant dye concentration of 500 mg L⁻¹. The adsorption capacity q_t (mg/g) and removal rate (%) were calculated according to the following equation.

$$Q_t = \frac{(C_0 - C_t)}{m} \times V \quad (1)$$

$$\eta = \frac{C_0 - C_t}{C_0} \times 100\% \quad (2)$$

Where C_0 is the initial solution concentration (mg g⁻¹), and C_t is the solution concentration at time t , V is the volume of solution (L) and m is the weight of MoG (g).

1.3 Evaporation rate measurement via solar simulator

In order to quantify the real-time weight variation of water throughout the solar-driven evaporation process, a beaker containing water was positioned atop a precision balance accurate to four decimal places. This setup allowed for the assessment of both the evaporation rate and solar-thermal conversion efficiency. A segment of aerogel was positioned on the water's surface. Utilizing a 300 W xenon lamp coupled with an AM 1.5 G filter as the solar illumination source, the light intensity was measured employing a robust light photometer. The simulated solar irradiance (1000 W m⁻²) was directed perpendicularly onto the floating aerogel. The steam generation efficiency (η) was also employed as a metric to gauge the desalination efficacy of the MoG aerogel, and it can be evaluated using the subsequent formula.¹

$$\eta = \frac{kh_{LV}}{C_{opt} \times q_i} \quad (3)$$

where k is the evaporation rate, h_{LV} is the enthalpy of water evaporation (2444 J/g), C_{opt} is the optical concentration and q_i is the normal solar irradiation (100 mW cm⁻²).²

1.4 Energy calculation

In an effort to explain the extremely efficient utilization of the solar energy by the MoG evaporator, we conducted an in-depth analysis of energy losses using the following equation⁷:

$$Q_{sun} = Q_{evap} + Q_{loss} = S_{evap} D_a h_{fg} \left(C_{sat}(T_s) - \phi_{\infty} C_{sat}(T_{\infty}) \right) + A h_{loss} \Delta T \quad (4)$$

$$A \partial q''_{solar} = S_{evap} D_a h_{fg} \Delta c + A \varepsilon \sigma (T_s^4 - T_{\infty}^4) + A h_{conv} + \Delta T + \frac{\Delta T}{\frac{1}{S_{cond} K_1} + \frac{t_s}{A K_{wick}}} \quad (5)$$

In the equation (4), where S_{evap} , D_a , and A are the evaporative shape factor, vapor mass diffusivity in air, area of the evaporator, respectively. $C_{sat}(T_s)$ and $C_{sat}(T_{\infty})$ are vapor saturation concentrations at T_s and T_{∞} , respectively. ϕ_{∞} is the far-field relative humidity.

In the equation (5), where ∂ , ε , σ , h_{conv} , K_1 , and K_{wick} are the evaporator solar absorptance, evaporator infrared emissivity, Stefan–Boltzmann constant, convective heat loss coefficient, water thermal conductivity, and effective thermal conductivity of the capillary wick, respectively. $S_{cond} = 2D$ is the conductive shape factor for a circular-disk evaporator. $h_{conv} = 1 / (1/h_a + 1/h_c)$ includes the contributions of both the heat transfer coefficient of air ambient (h_a) and convection cover (h_c).

For the MoG evaporator, A_{top} is 4 cm^2 , T_{top} is $35.8 \text{ }^{\circ}\text{C}$, A_{side} is 4 cm^2 , and T_{side} is $30.5 \text{ }^{\circ}\text{C}$, $T_{environment}$ is the ambient temperature ($25 \text{ }^{\circ}\text{C}$), ε is emissivity of the absorbing surface (~ 0.98), σ is the Stefan-Boltzmann constant ($5.67 \times 10^{-8} \text{ W m}^{-2} \text{ K}^{-4}$), h is convection heat transfer coefficient (assumed to be $5 \text{ W m}^{-2} \text{ K}^{-1}$), Since the side evaporation surface has a lower temperature than the environment temperature, it could gain energy from the environment.

According to the above equation, for the MoG evaporator, the radiation loss from the top evaporation surface was estimated to be 0.0254 W, the radiation energy loss of the side evaporation surface was 0.0211 W, while radiation energy gain of the cotton side evaporation surface from surrounding environment was 0.0235 W; Convection loss from the top evaporation surface was estimated to be 0.0198 W, convection loss from the side evaporation surface was estimated to be 0.0176 W and convection energy gain of the MoG-based aerogel side evaporation surface from surrounding environment was estimated to be 0.0873 W.

Therefore, the evaporator has a net energy gain of 0.0269 W from the environment.”

1.5 Photothermal antibacterial tests

Bacteria *Escherichia coli* (*E. coli*) was cultured in Luria-Bertani (LB) liquid medium at 37 °C for 6 hours. Subsequently, the culture was dispersed using glass beads and diluted by a factor of 10^5 with LB medium. Then, 100 microliters of the diluted *E. coli* solution were applied to coat a Petri dish. The dish was placed under 1 sunlight for 60 minutes, thereafter, the LB solid medium, following the experimental procedure, was cultured at 37 °C for 14 hours. Finally, the size of the antibacterial zone was measured.

1.6 Evaluation of nanofiltration performance

MoG colloidal solutions were deposited onto nylon substrates using a straightforward vacuum filtration technique. During the vacuum filtration process, the nylon membrane was initially wetted with water and then affixed to the sand core of the suction filtration apparatus using a large holder. Subsequently, a highly dispersed MoG solution was gently poured onto the surface of the nylon membrane, achieving a loading mass of

7.64 mg cm⁻². The volume of the colloidal solutions (3 mg/ml) was precisely controlled at 50 ml. Simultaneously, a vacuum pump was engaged to facilitate the permeation of the liquid through the porous nylon membrane until no visible liquid remained on the membrane's surface. Each membrane underwent triplicate analyses under identical conditions. The nanofiltration efficacy was evaluated through dead-end filtration experiments involving diverse dyes and Hg²⁺ solutions (50 ppm). The concentrations of the feed and permeate were determined using ultraviolet-visible (UV-Vis) spectroscopy, with measurements taken at the respective maximal absorption wavelengths of the six organic dyes.

Filtration characteristics, including water permeability (J, L m⁻² h⁻¹ bar⁻¹) and dye rejection (R, %), were calculated by the following equations:

$$J = \frac{J_w}{\Delta P} = \frac{V}{A \times t \times \Delta P} \quad (6)$$

Where V is the volume of permeate (L), A is effective membrane area (4×10^{-4} m²), t is the permeation time (h), and ΔP is the transmembrane pressure (0.8 bar).

$$R_{\%} = \frac{C_f - C_p}{C_f} \times 100 \quad (7)$$

Where C_f and C_p are the concentrations of markers in the permeate and retentate solutions.

A synthetic sewage was prepared to mimic a real application scenario to determine the purification ability of the system:³ a suitable amount of biological and chemical medium, consisting of 80 mg of peptone, 55 mg of meat extract, 15 mg of urea, 14 mg of K₂HPO₄, 4 mg of NaCl, 2 mg of CaCl₂·2H₂O, and 1 mg of Mg₂SO₄·7H₂O, were dissolved in 500 mL of tap water.

1.7 Cascade system and traditional wastewater treatment process inventory

Cascade system: It is mentioned in the text that the average water evaporation of our cascade system is $1.32 \text{ kg m}^{-2} \text{ h}^{-1}$, and the area of the gel evaporator required when the water yield is 5000 L/h is calculated according to equation S6:

$$\text{Aerogel area}(A_a, \text{m}^2) = \frac{Q_e}{Q_a} \quad (8)$$

The volume of the gel evaporator is given by equation S7, where the aerogel thickness is assumed to be 1 cm.

$$\text{Aerogel volume}(A_v, \text{m}^3) = 0.01 \times \text{Aerogel area} \quad (9)$$

In addition, the average density of MoG loaded on the aerogel is 200 kg/m^3 , so equation S8 can be used to calculate the total amount of MoG required for a gel evaporator with a water volume of 5000 L/h.

$$\text{MoS}_2\text{-g-C}_3\text{N}_4 \text{ mass}(\text{MoG m, kg}) = 200 \times \text{Aerogel volume} \quad (10)$$

The average density of MoG loaded on the membrane is 9.43 kg/m^2 , and the water flux of the membrane is $966 \text{ L m}^{-2} \text{ h}^{-1} \text{ bar}^{-1}$, so equation S9 can be used to calculate the total amount of MoG required by the filter membrane when the water volume is 5000 L/h.

$$\text{MoS}_2\text{-g-C}_3\text{N}_4 \text{ mass}(\text{MoG m, kg}) = \frac{Q_e}{L_m} \times 9.43 \quad (11)$$

By modeling the MoG synthesis process using the ecoinvent v3.5 database, the CO_2e for the production of 1 kg of MoG was calculated.

1.8 Traditional wastewater treatment process

The traditional process includes pretreatment, conditioning and oxidation, Adsorption, coagulation and filtration. Each step of the process requires the addition of chemical

agents. The environmental benefits of traditional processes are determined by calculating the amount of carbon dioxide generated during the production of the chemical agents. Including FeCl₃, PAM (polyacrylamide), lime, activated carbon, manganese sand, KDF copper-zinc alloy filter media. The dosage of each chemical agent for each step of the process is known from the literature.

1.9 Janus graphene oxide evaporator inventory:

Evaporation rate: The reported E.R. was extracted from Fig. 8e from Lin et al. and estimated at a value of 0.74 kg m⁻² h⁻¹. This can be used as the true evaporation rate under real sunlight.

In order to achieve a better comparison, we specify that the required area is calculated based on the 1 L/h water discharge rate, which can be calculated according to equation S10.

$$\text{Janus evaporator area (JEa, m}^2\text{)} = \frac{Q_e}{Q_a} \quad (11)$$

The volume of the Janus GO evaporator is given by equation S11, where the thickness of the evaporator is assumed to be 1 cm.

$$\text{Janus evaporator volume (JEv, m}^3\text{)} = 0.01 \times \text{Janus evaporator area} \quad (12)$$

In addition, the average density of the Janus GO evaporator is 280 kg/m³, so Equation S7 can be used to calculate the total mass of the gel evaporator at 1 L/h of water.

$$\text{Janus evaporator mass (JEm, kg)} = 280 \times \text{Janus evaporator volume} \quad (13)$$

By modeling the Janus GO evaporator synthesis process using the Ecoinvent v3.5 database, the CO_{2e} for the production of 1 kg of Janus GO evaporator was calculated.

Similarly, the total mass of other evaporators can also be calculated according to the above method, and the specific parameters are detailed in Table S6.

Supporting Figures

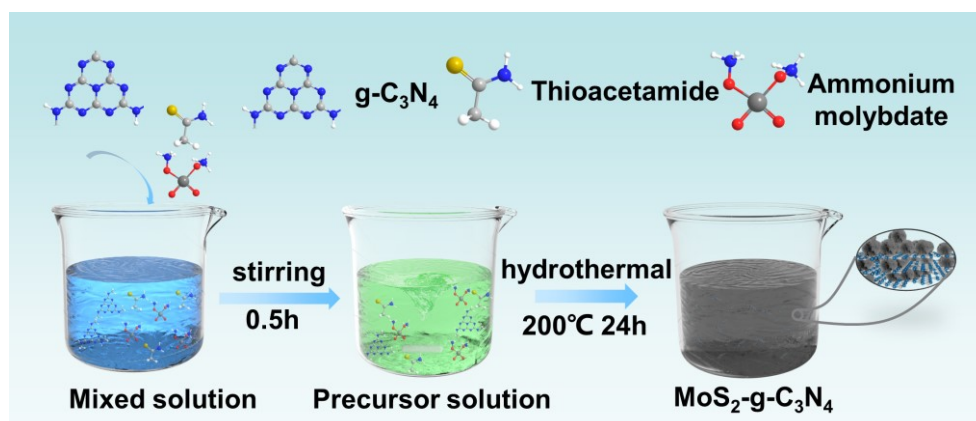


Figure S1 Schematic diagram for the preparation of MoG using a hydrothermal method.

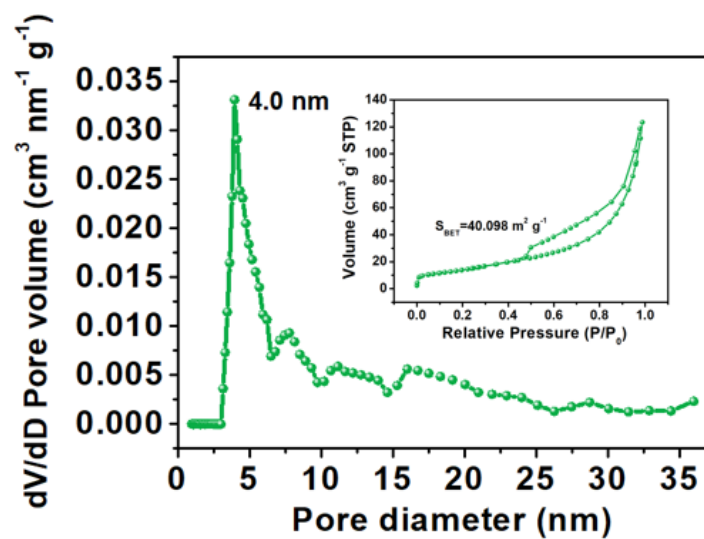


Figure S2 Size distribution of MoG mesoporous structure (inset is N_2 adsorption-desorption isotherm).

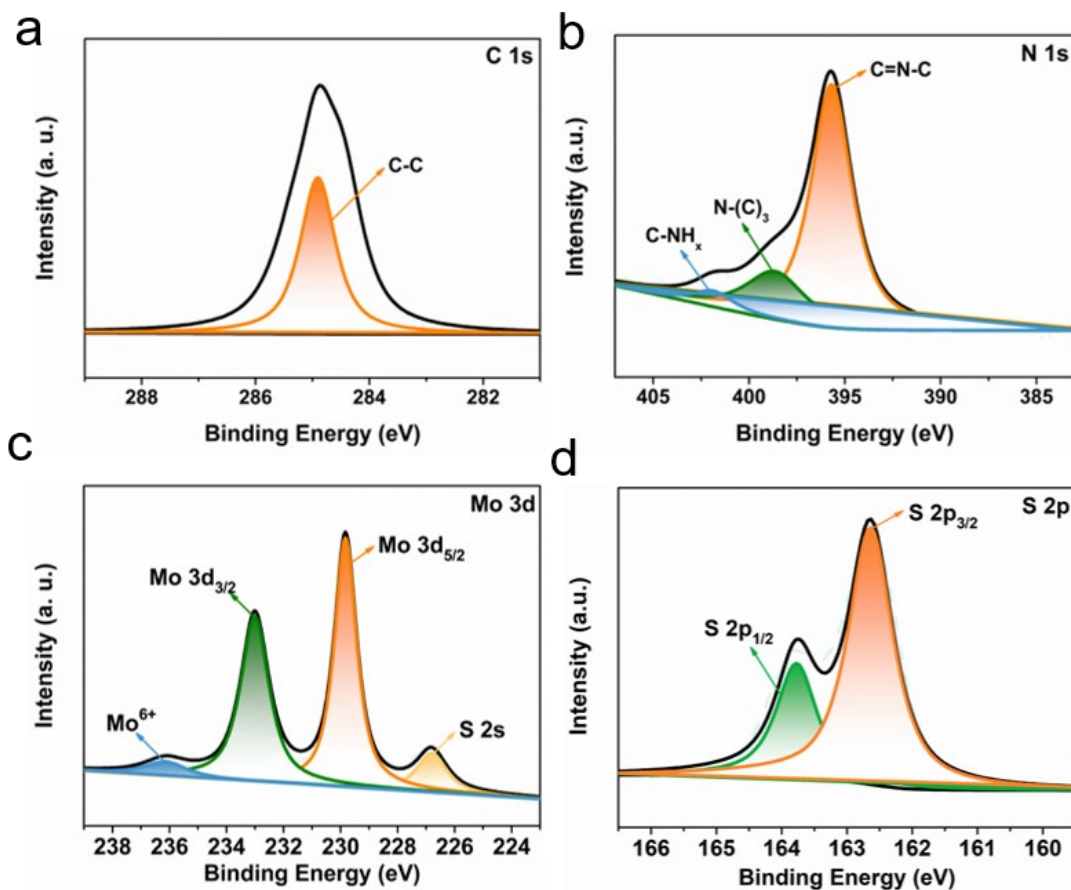


Figure S3 XPS spectra of (a) C 1s, (b) N 1s, (c) Mo 3d and (d) S 2p.

The C 1s XPS spectrum exhibited distinct peaks at ~ 284.8 eV, corresponding to the graphitic adventitious C-C bond within g-C₃N₄. In the N 1s spectrum, three peaks emerged at ~ 400.6 , ~ 399.6 , and ~ 398.2 eV, attributed to C-NH_x, N-(C)₃, and C=N-C functionalities, respectively. Within the S 2p spectrum, the prominent peaks at ~ 163.08 eV (S 2p_{1/2}) and ~ 161.87 eV (S 2p_{1/2}) signify the presence of the 1 T phase. Two smaller peaks at around 163.68 and 162.5 eV are assigned to the S 2p_{1/2} and S 2p_{3/2} orbitals of the 2 H phase, respectively⁴. To validate the existence of the 1 T phase MoS₂, the Mo 3d and S 2p XPS spectra were subjected to analysis. Notably, two principal peaks at ~ 232.3 and ~ 228.9 eV correspond to Mo⁴⁺ 3d_{3/2} and Mo⁴⁺ 3d_{5/2} orbitals within the 1 T phase, respectively. Simultaneously, the minor peaks at around 232.6 and 229.5 eV are

indicative of the $\text{Mo}^{4+} 3d_{3/2}$ and $\text{Mo}^{4+} 3d_{5/2}$ orbitals within the 2H phase, respectively. Furthermore, an additional peak at ~ 235.7 eV is attributed to Mo^{6+} within MoO_3 , stemming from coordination-induced slight oxidation. The S 2s peak is positioned at ~ 226.3 eV. It is of significance to highlight that within the S 2p spectrum of MoG, a distinct peak at 164.1 eV signifies the presence of S-C bonds, consistent with existing literature.⁵⁻⁷ This peak was attributed to the reaction of S atoms with the functional groups and with the edges of g- C_3N_4 , resulting in a bridge between g- C_3N_4 and the MoS_2 nano spheres.

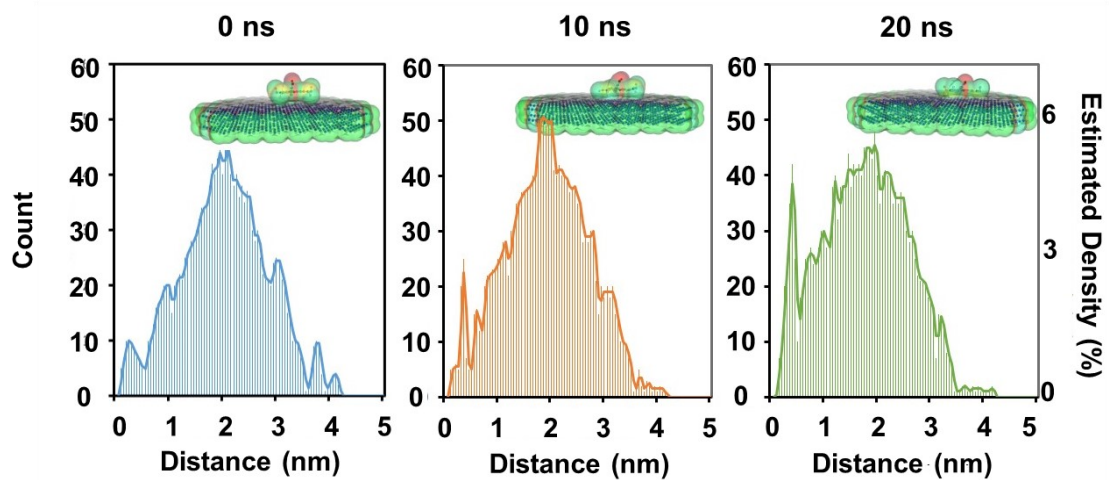


Figure S4 Molecular dynamic simulation of the interaction g-C₃N₄ and rhodamine B. Histograms and estimated densities of the distance between the atoms of rhodamine B and the surface of g-C₃N₄ at 0 (blue), 10 (yellow), and 20 (green) ns respectively.

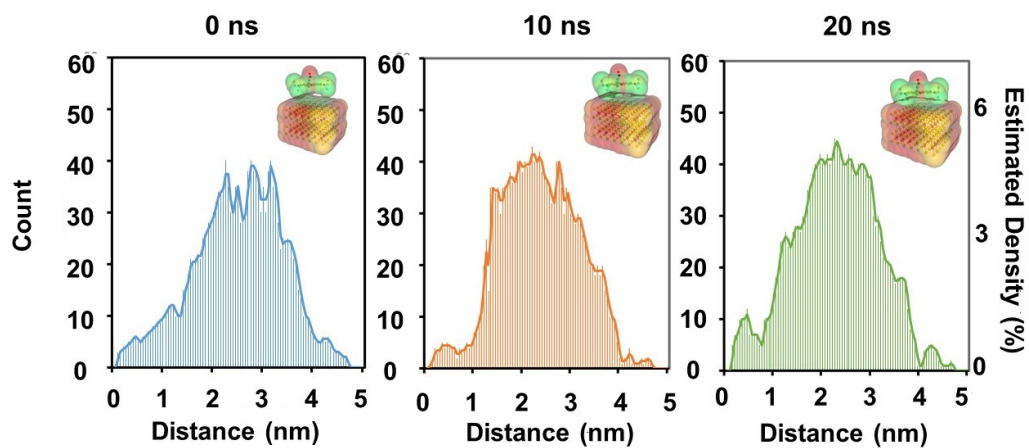


Figure S5 Molecular dynamic simulation of the interaction MoS₂ and rhodamine B . Histograms and estimated densities of the distance between the atoms of rhodamine B and the surface of MoS₂ at 0 (blue), 10 (yellow), and 20 (green) ns respectively.

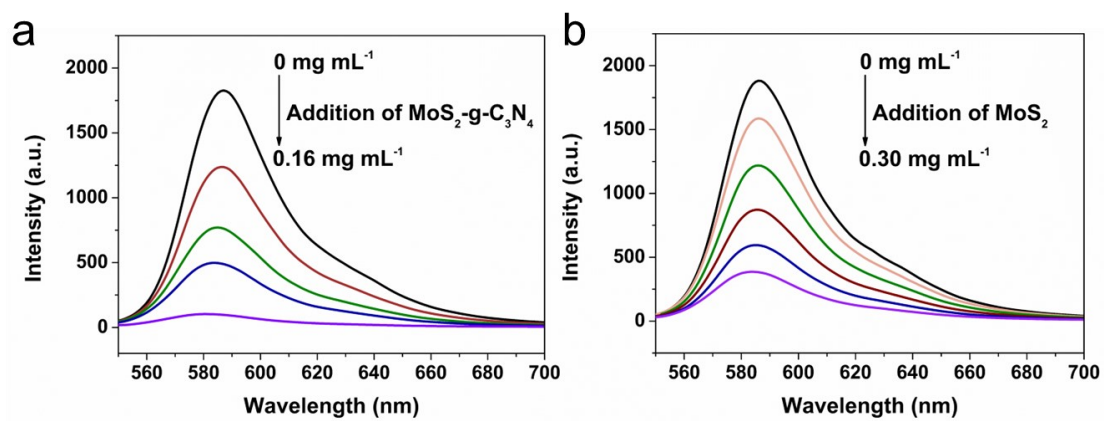


Figure S6 (a) Fluorescence spectra of RhB titrated with MoG; **(b)** Fluorescence spectra of RhB titrated with MoS₂.

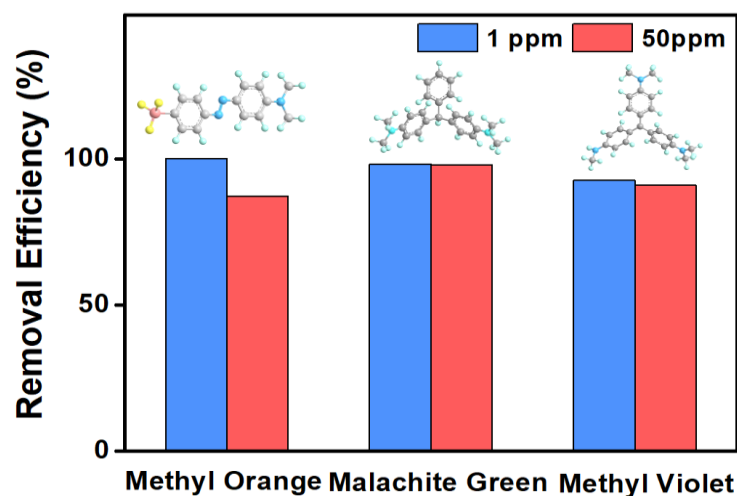


Figure S7 Comparison of adsorption efficiency for different dyes at different concentrations.

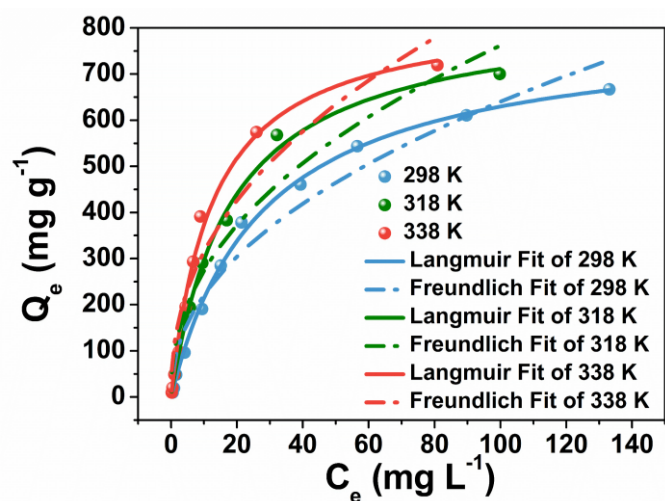


Figure S8 Adsorption isotherms of RhB by MoG at different temperatures.

We first investigated the effect of temperature on the adsorption of RhB by MoG, experimental studies were carried out at 298 K, 318 K, 338 K respectively. From the correlation coefficients (R^2) and fitting curves (Table S1), it was found that the Langmuir model is more suitable to simulate RhB adsorption than the Freundlich model, indicating a monolayer coverage of adsorbents.⁸

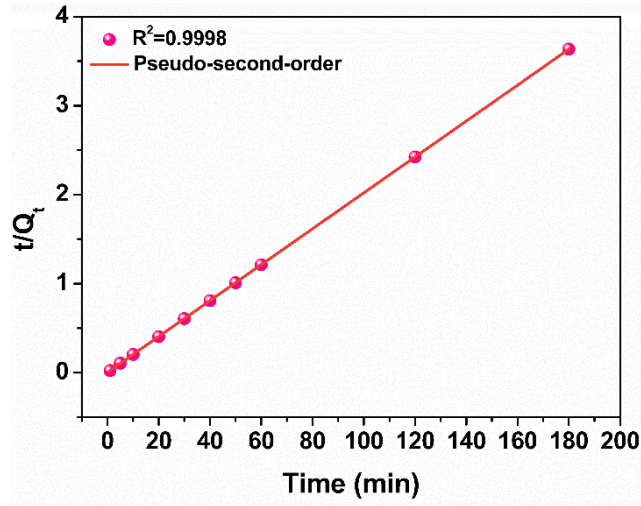


Figure S9 Pseudo-secondary kinetic model for RhB adsorption; ($C_0 = 500$ ppm; $T = 298$ K; m adsorbent = 10 mg; $V = 10$ mL).

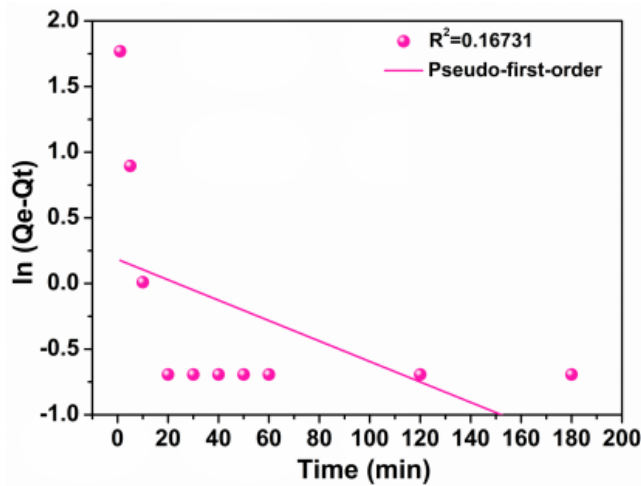


Figure S10 Fitting results for pseudo-first-order.

The fitting results and kinetic parameters are shown in Table S2. The results from Table S2 show that the linear pseudo-second-order kinetic model, with the highest R^2 (0.9998), is more consistent with the experimental data than the other models.

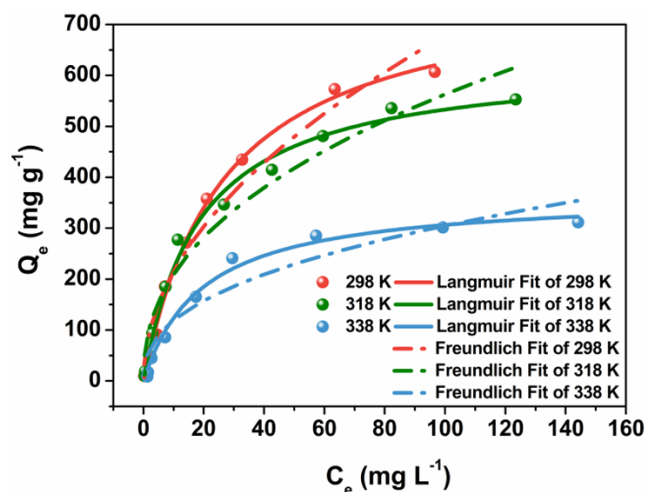


Figure S11 Adsorption isotherms of Hg^{2+} by MoG at different temperatures.

To further explore the influence of temperature on mercury ion adsorption by MoG, experimental studies were carried out at 298 K, 318 K, 338 K respectively. The Langmuir and Freundlich adsorption isotherm models are used to fit the experimental data. The values of q_m , K_L , K_F and n displayed in Table S3. According to the fitting curve and correlation coefficient (R^2), the former R^2 was larger than the latter R^2 , indicating that Langmuir model was more suitable for simulating Hg^{2+} adsorption than Freundlich model.

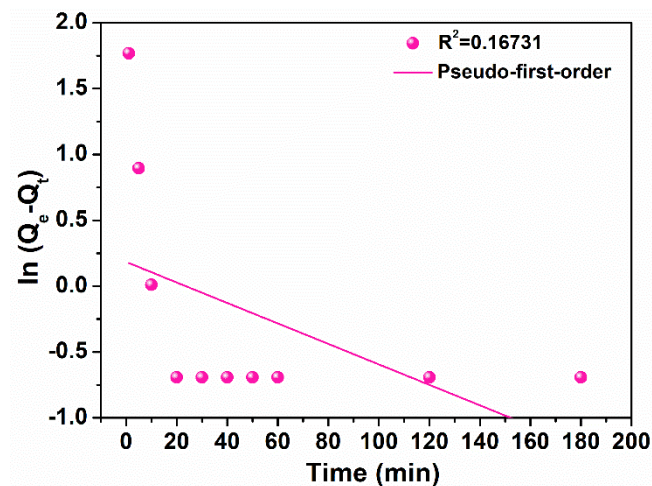


Figure S12 Fitting results for pseudo-first-order.

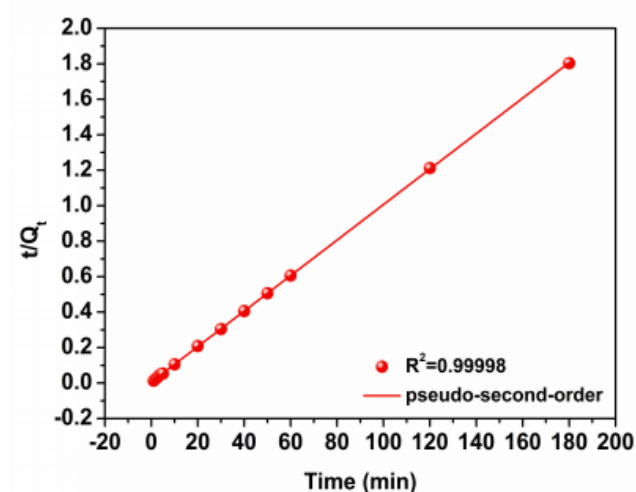


Fig. S13 Fitting results for pseudo-second-order.

Identically, the fitting results and kinetic parameters of kinetic models are shown in Table S4. Obviously, the linear correlation coefficient ($R^2 = 0.9998$) for the pseudo-second-order model is higher than the linear correlation coefficient ($R^2 = 0.16731$) for the pseudo-first-order one. This result indicates that chemisorption is the dominant adsorption process of Hg^{2+} .

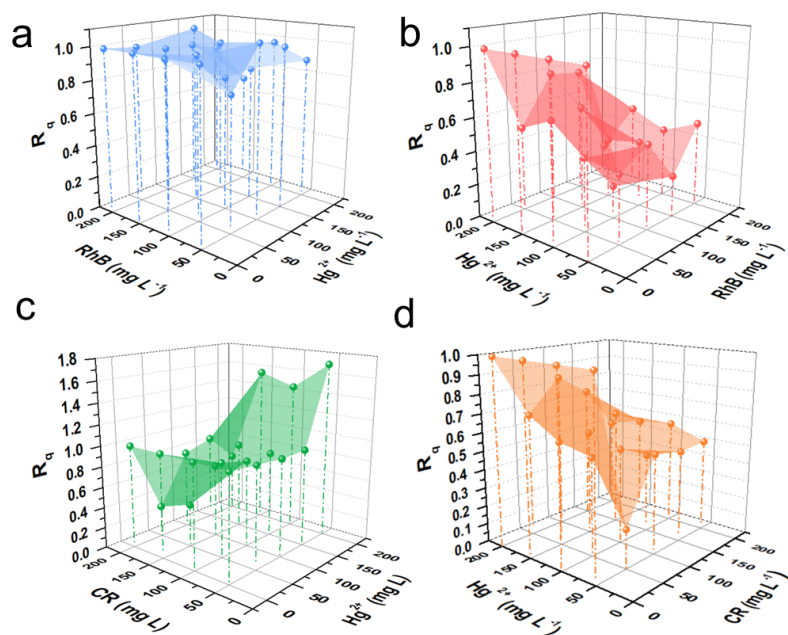


Figure S14 (a-d) Simultaneous adsorption of Hg^{2+} /RhB and Hg^{2+} / Congo red (CR) by MoG.

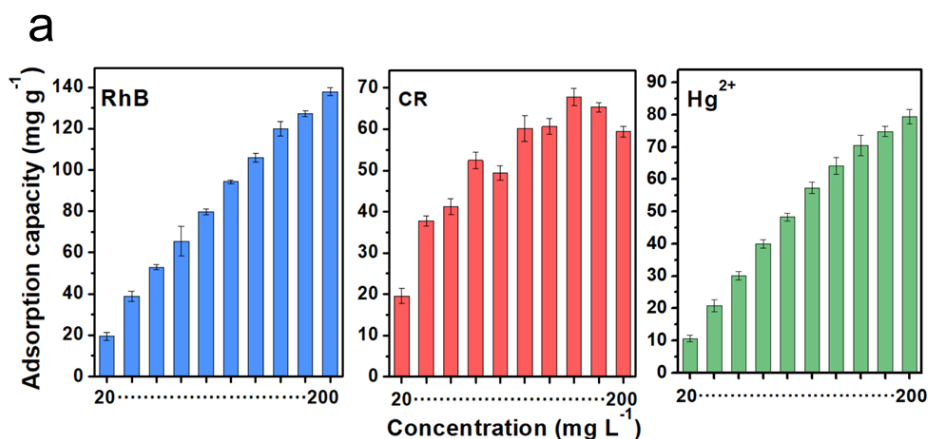


Figure S15 Simultaneous adsorption capacity of RhB, CR, Hg^{2+} by MoG at different initial concentrations.

In the context of the RhB- Hg^{2+} cationic system, the $R_{q,RhB}$ values (Fig. S14a) closely approached 1, indicating minimal influence of coexisting Hg^{2+} on RhB adsorption. Conversely, the $R_{q,Hg^{2+}} < 1$ (Fig. S14b), signifying varying degrees of inhibition in Hg^{2+} adsorption by RhB. This is because RhB carries a positive charge when dissolved in water, allowing for electrostatic attraction with the negatively charged MoS_2 .⁹ Additionally, MoS_2 possesses inherent polarization at its edge active

sites, enabling interactions with specific polar molecules such as RhB. This implies that the binding force between the adsorbent and RhB is greater than that between Hg^{2+} , resulting in this phenomenon.¹⁰⁻¹²

In the context of the CR- Hg^{2+} anionic system, the $R_{q,\text{CR}} \geq 1$ (Fig. S14c) means that the presence of Hg^{2+} substantially augmented the CR removal process. Conversely, Hg^{2+} adsorption experienced varying degrees of inhibition by CR (Fig. S14d). This phenomenon can be rationalized as follows: CR, a negatively charged anionic dye in aqueous solution, may achieve enhanced adsorption by the formation of a VI-Hg-CR configuration facilitated through Hg^{2+} bridging.¹³ In ternary systems, the adsorption capacity exhibited the sequence of $\text{RhB} > \text{Hg}^{2+} > \text{CR}$ (Fig. S15a), a trend congruent with outcomes from single-species adsorption investigations. It was worth noting, CR adsorption achieved peak levels before diminishing at higher concentrations, potentially attributable to a reduction in accessible adsorption sites within the ternary milieu. Notably, relative to their respective single adsorption systems, MoG displayed diminished adsorption capacity for these metallic ions. Within the ternary systems, escalating concentrations of metal ions engendered competitive adsorption onto MoG, consequently inducing a decline in removal efficiency. On the basis of the above experimental phenomena, we suspect that the high efficiency of the MoG upon pollutant elimination is due to the synergistic effect of physical adsorption and chemical adsorption. Considering the molecular architectures of RhB and MoG, an electrostatic interaction between RhB and MoG arises. This stems from the cationic nature of RhB and the negative charge carried by MoG within the solution. Furthermore, both RhB

and MoG encompass aromatic rings, thus potentially engendering heightened π - π interactions. Moreover, the presence of nitrogen atoms in both g-C₃N₄ and RhB opens the possibility for hydrogen bonding between these constituents. The adsorption of CR by the MoG could be attributed to the open hierarchical structure of the composite.¹⁴ Meanwhile, the adsorption mechanisms of the Hg²⁺ on MoG were mainly the chelation between S and Hg on the adsorbent-adsorbate interface as well as precipitation and crystal growth on the surface of the adsorbent.¹⁵

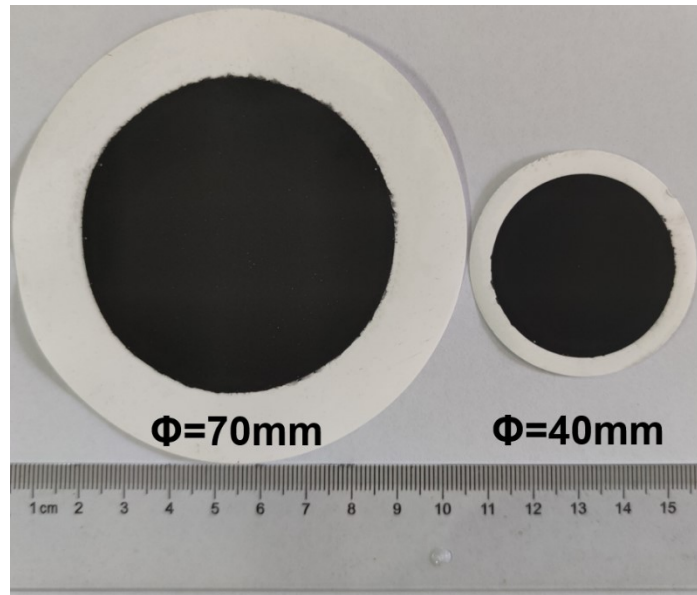


Figure S16 Example of a large-area MoG/nylon membrane fabricated by vacuum filtration.

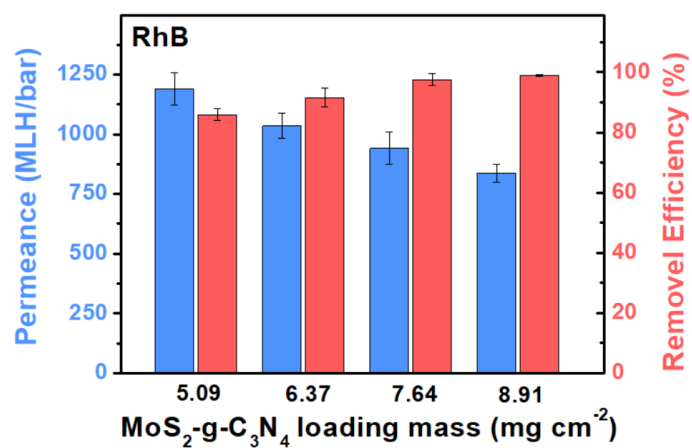


Figure S17 Removal efficiency and water flux of MoG membrane for RhB at different loading levels.

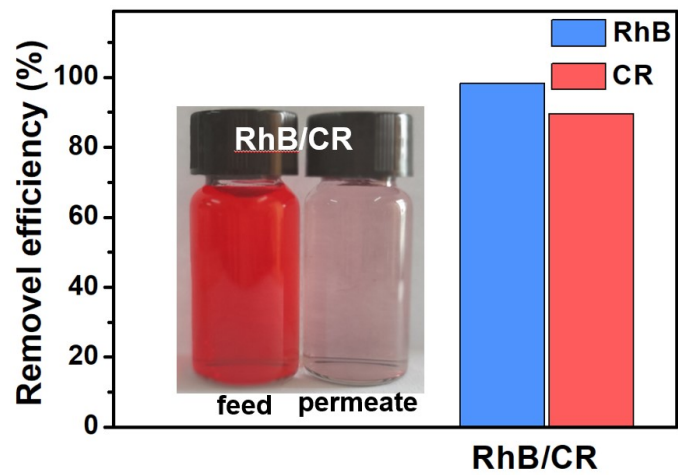


Figure S18 Separation performance of MoG for mixed dye molecules of Rhodamine B/Congo red (RhB/CR).

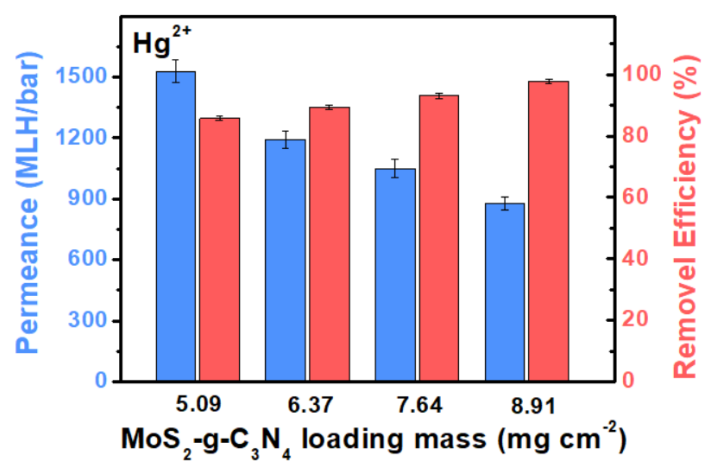


Figure S19 Removal efficiency and water flux of MoG membrane for Hg²⁺ at different loading levels.

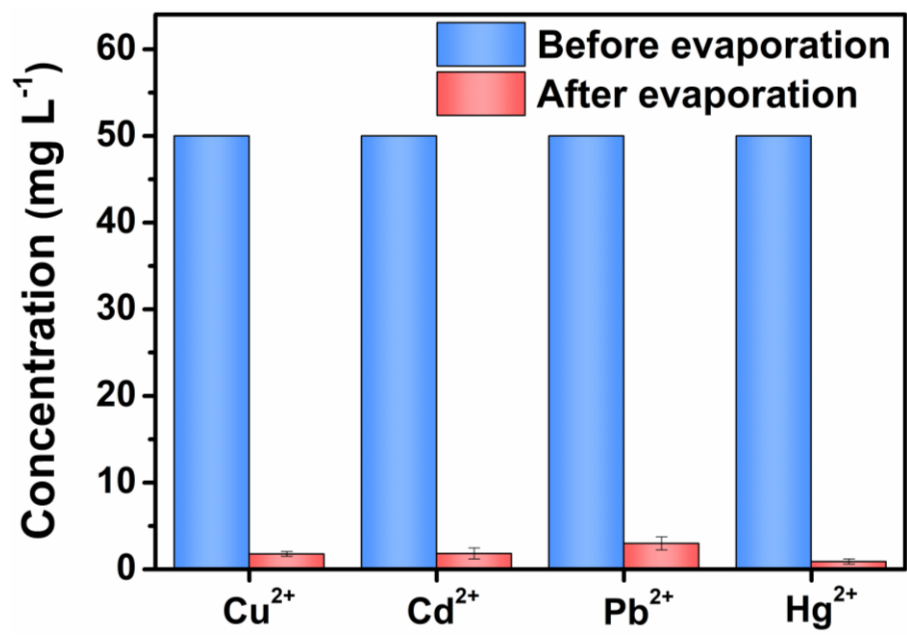


Figure S20 Concentration of heavy metal ions in water after evaporation.

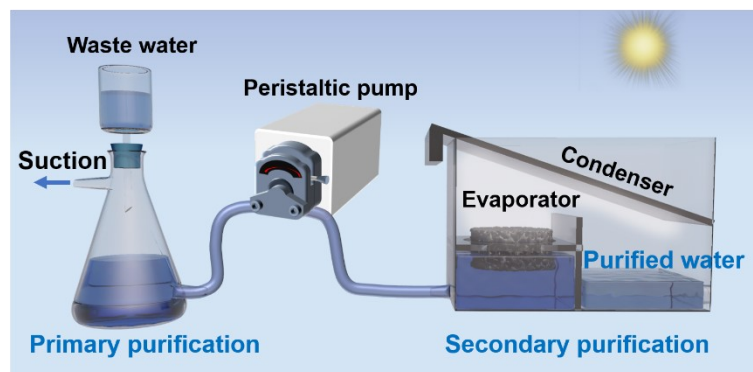


Figure S21 Schematic diagram of the two-stage interconnected system for clean water production.

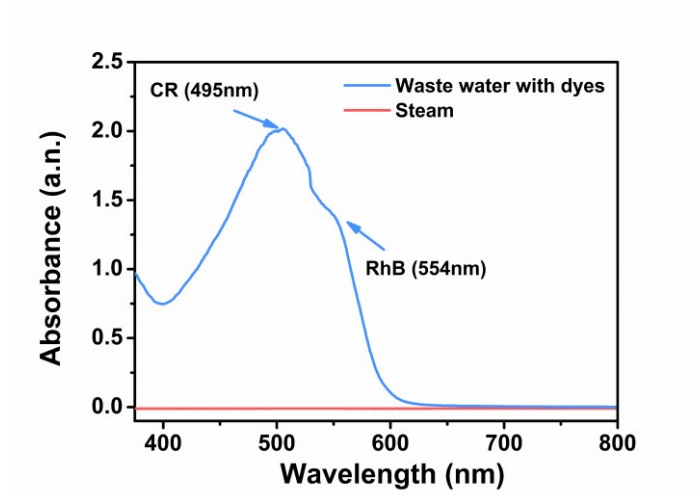


Figure S22 The UV absorption spectra of dyes in simulated wastewater before and after solar evaporation.

Table S1. Parameters for isotherm models for the sorption of RhB on MoG.

T, K	Langmuir			Freundlich		
	q_m , mg/g	K_L , L/mg	R^2	K_f	n	R^2
298	777.6347	0.03895	0.996	73.2208	2.1487	0.958
318	802.170	0.05945	0.987	100.0000	2.2321	0.951
338	775.789	0.09129	0.985	115.718	2.3460	0.927

Table S2. Adsorption parameters of RhB.

C_0 , mg/L	q_m , mg/g	pseudo-first-order			pseudo-second-order		
		K_1 , min ⁻¹	q_e , mg/g	R_1^2	K_2 , mg g ⁻¹ min ⁻¹	q_e , mg/g	R_2^2
50	49.8	0.0253	1.2016	0.6362	0.2580	49.5295	1.00 0

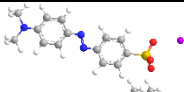
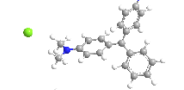
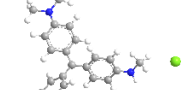
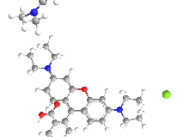
Table S3. Parameters for isotherms models for the sorption of Hg²⁺ on MoG.

T, K	Langmuir			Freundlich		
	q_m , mg/g	K_L , L/mg	R^2	K_f	n	R^2
298	768.116	0.02429	0.987	39.3228	1.9209	0.850
318	781.476	0.00654	0.995	16.6213	1.6349	0.971
338	923.012	0.00365	0.996	9.9986	1.4646	0.986

Table S4. Adsorption parameters of Hg²⁺ ions.

C_0 , mg/L	q_m , mg/g	pseudo-first-order			pseudo-second-order		
		K_1 , min ⁻¹	q_e , mg/g	R_1^2	K_2 , mg g ⁻¹ min ⁻¹	q_e , mg/g	R_2^2
100	99.8	0.0253	10.7145	0.6362	0.0169	100	0.999

Table S5. Chemical structures and sizes of six dye molecules used in this research.

	Molecular weight (g mol ⁻¹)	Solute Charge	Chemical structure
Methyl orange (MO)	327.33	-	
Malachite green (MG)	364.91	+	
Methyl violet (MV)	408.03	+	
Rhodamine B (RhB)	479.01	+	

Bromocresol purple (BP)	540.22	-	
Methyl Blue (MB)	799.8	-	

Table S6. Evaporator parameters.

	Evaporation rate ($\text{kg m}^{-2} \text{h}^{-1}$)	Thickness (m)	Mass density (kg/m^3)	References
J-PPy	0.6175	0.01	254.7	16
PSHs	2.1	0.01	86.7	17
COF/GO	3.69	0.01	13.46	18
PDMX/HPP	1.08	0.016	178	19
PPy-PI NAG	1.42	0.01	35.7	19
MTBs	0.68	0.01	217	20

Table S7. WHO standard for drinking water.

Heavy metal	Mercury	Cadmium	Lead	Copper	Turbidity
WHO Guideline value (mg L^{-1})	0.001	0.005	0.01	2	5NTU

Table S8. Estimation of materials cost for cascade system.

Chemicals	Vendor	Price		Materials/ device	Price/ device
		Quantity	Price		
Thioacetamide	Kermel	500 g	\$ 40.3	0.135 g	\$ 0.01
Ammonium molybdate tetrahydrate	Kermel	500 g	\$ 22.8	0.175 g	\$ 0.0008
Melamine	Macklin	500 g	\$ 12.8	0.0175 g	\$ 0.0004
Chitosan	TCL	500 g	\$ 67.1	0.2 g	\$ 0.03
Nylon membrane	Zhejiang Yibo	1 m^2	\$ 96	0.002 m^2	\$ 0.192
Acetic acid	Kermel	500 mL	\$ 5.8	0.2mL	\$ 0.002
Glutaraldehyde (25%)	Kermel	500 mL	\$ 9	1 mL	\$ 0.018
Operating cost		1 kW h	\$ 0.05	96.08 kW h	\$ 4.804
Cost of cascade system					\$ 5.22

Reference

- 1.Y. Zhang, X. Yin, B. Yu, X. Wang, Q. Guo and J. Yang, Recyclable polydopamine-functionalized sponge for high-efficiency clean water generation with dual-purpose solar evaporation and contaminant adsorption, *ACS Appl. Mater.*, 2019, **11**, 32559-32568.
- 2.X. Zhang, L. Yang, B. Dang, J. Tao, S. Li, S. Zhao, W. Li, J. Li, Z. Chen and S. Liu, Nature-inspired design: p-toluenesulfonic acid-assisted hydrothermally engineered wood for solar steam generation, *Nano Energy*, 2020, **78**, 105322.
- 3.F. Zhao, E. Repo, D. Yin, Y. Meng, S. Jafari and M. Sillanpää, EDTA-Cross-linked β -cyclodextrin: an environmentally friendly bifunctional adsorbent for simultaneous adsorption of metals and cationic dyes, *Environ. Sci. Technol.*, 2015, **49**, 10570-10580.
- 4.X. Liu, X. Han, Z. Liang, Y. Xue, Y. Zhou, X. Zhang, H. Cui and J. Tian, Phosphorous-doped 1T-MoS₂ decorated nitrogen-doped g-C₃N₄ nanosheets for enhanced photocatalytic nitrogen fixation, *J. Colloid. Interface. Sci.*, 2022, **605**, 320-329.
- 5.M. Kawase, K. Akaike, K. Aoyama, Y. Ito, M. Tamura and K. Kanai, Elucidation of the enhanced photoactivity of melon calcined with MoO₃, *Appl. Catal. B*, 2020, **273**, 119068.
- 6.J. K. Hedlund and A. V. Walker, Modulating the electronic properties of Au-MoS₂ interfaces using functionalized self-assembled monolayers, *Langmuir*, 2020, **36**, 682-688.
- 7.B. Wang, Y. Zhang, J. Zhang, R. Xia, Y. Chu, J. Zhou, X. Yang and J. Huang, Facile synthesis of a MoS₂ and functionalized graphene heterostructure for enhanced lithium-storage performance, *ACS Appl. Mater. Interfaces*, 2017, **9**, 12907-12913.
- 8.M. Li, B. Wang, M. Yang, Q. Li, D. G. Calatayud, S. Zhang, H. Wang, L. Wang, B. J. S. Mao and P. Technology, Promoting mercury removal from desulfurization slurry via S-doped carbon nitride/graphene oxide 3D hierarchical framework, *Sep. Purif. Technol.*, 2020, **239**, 116515.
- 9.Y. Fang, Q. Huang, P. Liu, J. Shi and G. Xu, Easy-separative MoS₂-glue sponges with high-efficient dye adsorption and excellent reusability for convenient water treatment, *Colloids Surf. A Physicochem. Eng. Asp.*, 2018, **540**, 112-122.
- 10.X. Xiao, Y. Wang, B. Cui, X. Zhang, D. Zhang and X. Xu, Preparation of MoS₂ nanoflowers with rich active sites as an efficient adsorbent for aqueous organic dyes, *New J. Chem.*, 2020, **44**, 4558-4567.
- 11.X. Zhao, J. Bao, Y. Zhou, Y. Zhang, X. Sheng, B. Wu, Y. Wang, C. Zuo and X. Bu, Heterostructural MoS₂/NiS nanoflowers via precise interface modification for enhancing electrocatalytic hydrogen evolution, *New J. Chem.*, 2022, **46**, 5505-5514.
- 12.N. T. Thang, L. T. Hong, N. H. Thoan, C. M. Hung, N. Van Duy, N. Van Hieu and N. D. Hoa, Controlled synthesis of ultrathin MoS₂ nanoflowers for highly enhanced NO₂ sensing at room temperature, *RSC Adv.*, 2020, **10**, 12759-12771.
- 13.I. M. Alarifi, Y. O. Al-Ghamdi, R. Darwesh, M. O. Ansari and M. K. Uddin, Properties and application of MoS₂ nanopowder: characterization, Congo red

- dye adsorption, and optimization, *J. Mater. Res. Technol.*, 2021, **13**, 1169-1180.
- 14.X. Huang, X. Xu, R. Yang and X. Fu, Synergetic adsorption and photocatalysis performance of g-C₃N₄/Ce-doped MgAl-LDH in degradation of organic dye under LED visible light, *Colloids Surf. A Physicochem. Eng. Asp.*, 2022, **643**, 128738.
- 15.X. Zhao, J. Li, S. Mu, W. He, D. Zhang, X. Wu, C. Wang and H. Zeng, Efficient removal of mercury ions with MoS₂-nanosheet-decorated PVDF composite adsorption membrane, *Environ. Pollut.*, 2021, **268**, 115705.